Author/s:
Black, MT;Lane, TP

Title:
An improved diagnostic for summertime rainfall along the eastern seaboard of Australia

Date:
2015-12-01

Citation:
Black, M. T. & Lane, T. P. (2015). An improved diagnostic for summertime rainfall along the eastern seaboard of Australia. International Journal of Climatology, 35 (15), pp.4480-4492. https://doi.org/10.1002/joc.4300.

Persistent Link:
https://hdl.handle.net/11343/214424

INTERNATIONAL JOURNAL OF CLIMATOLOGY
RMetS Royal Meteorological Society

An improved diagnostic for summertime rainfall along the eastern seaboard of Australia

Journal:	*International Journal of Climatology*
Manuscript ID:	JOC-13-0581.R2
Wiley - Manuscript type:	Research Article
Date Submitted by the Author:	n/a
Complete List of Authors:	Black, Mitchell; University of Melbourne, School of Earth Sciences Lane, T; University of Melbourne, School of Earth Sciences
Keywords:	Australian Rainfall Variability, Geostrophic Flow, Climate Modelling, East Coast Flow Index, Gridded Data, Teleconnections, Eastern Australian Seaboard

An improved diagnostic for summertime rainfall along the eastern seaboard of Australia

Mitchell T. Black[1] and Todd P. Lane[1]

[1]School of Earth Sciences and ARC Centre of Excellence for Climate System Science, The University of Melbourne, Australia.

Corresponding author: M. T. Black, School of Earth Sciences, University of Melbourne, Melbourne, Vic 3010, Australia. (email: mtblack@student.unimelb.edu.au, ph: +613 8344 6911)

Short title: Australian East Coast Flow Index

Abstract

The eastern seaboard of Australia (ESB) is a unique climate entity. A region of complex topography bound by the coastline and the ridge of the Great Dividing Range, the ESB exhibits distinctly different rainfall patterns to the rest of south-eastern Australia. As a large percentage of the Australian population resides along the ESB, understanding current and future rainfall variability in this region presents an important and difficult challenge. This challenge is compounded by the inability of most general circulation models to properly resolve the region.

This study presents a diagnostic for characterizing the variability in summertime rainfall along the ESB. This simple yet effective East Coast Flow Index (ECFI) infers easterly geostrophic flow from the meridional pressure gradient along the ESB, and vertical circulation from the upper-level ω field. The ECFI outperforms the common indices for drivers of rainfall variability, achieving statistically significant correlations with ESB summertime rainfall for a range of different timescales. The ECFI is shown to have great potential as a predictor for statistically downscaling rainfall along the ESB as 1) it provides a physical link between large-scale forcings and local precipitation responses, 2) is capable of capturing multiyear variability, and 3) is realistically represented by general circulation models. While the ECFI was designed for the summer months (December–February) it is still capable of performing well in the other seasons, especially spring (September–November).

1 Introduction

Understanding rainfall variability along the eastern seaboard of Australia (ESB) is of utmost importance as it is a region of social, economic and environmental significance. Bounded by the Great Dividing Range to the west and the Pacific Ocean to the east, the ESB has long been recognised as a different climatological entity to the rest of eastern Australia (*Drosdowsky*, 1993; *Timbal*, 2010). The unique

climate of the ESB is linked to the local topography, with the Great Dividing Range acting as a distinct zone of separation between the ESB and inland eastern Australia (Figure 1). Annual rainfall along the ESB is more than double that recorded inland, with highest rainfall totals occurring during summer (*Timbal*, 2010).

There is high inter-annnual and inter-decadal variability in rainfall along the ESB (e.g., *Gallant et al.*, 2007; *Timbal*, 2010; *Gergis and Ashcroft*, 2013; *Fenby and Gergis*, 2013; *Pepler et al.*, 2014). This variability is reflected in surface runoff and river flow, which in turn can have notable impacts on freshwater ecosystems, agricultural production and catchment reservoir levels. As approximately 40% of the country's population resides along the ESB there is a need to understand the variations in rainfall, both past and present, in order to develop an integrated approach to the management of the region's water resources.

Australian rainfall is affected by a complex interplay of large-scale drivers: the El Niño Southern Oscillation (ENSO) (*McBride and Nicholls*, 1983; *Nicholls et al.*, 1996, 1997; *Wang and Hendon*, 2007) and the Indian Ocean Dipole (IOD)(*Cai et al.*, 2009; *Ummenhofer et al.*, 2009; *Ashok et al.*, 2003), both of tropical origin, and the Southern Annular Mode (SAM)(*Hendon et al.*, 2007; *Meneghini et al.*, 2007; *Nicholls*, 2010), of extratropical origin. These drivers are not independent, with ENSO in particular appearing to exert influence on, or mutually interact with, some of the other drivers (*Risbey et al.*, 2009). ENSO represents the variations in sea surface temperatures (and atmospheric patterns) across the Pacific Ocean, with warm (El Niño) events producing below-average rainfall and often drought over much of northern and eastern Australia (*McBride and Nicholls*, 1983), while the reverse is true during cool (La Niña) events. Sea surface temperature changes in the northern Indian Ocean are represented by the IOD (*Saji et al.*, 1999), with negative phases of the index implying warmer waters near Australia, and hence increased rainfall. In the extratropics, the north-south shift in the belt of strong westerly winds (between about 30° and 60°S) is represented by the SAM, with the positive phase representing the contraction of the belt (and associated cold fronts and storm

activity) towards the pole (*Meneghini et al.*, 2007). Although these three indices have well-known associations with rainfall in the Australian region, they are unable to explain summertime rainfall variability in eastern Australia, especially along the coast (e.g., see *McBride and Nicholls*, 1983; *Risbey et al.*, 2009).

The Coral and north Tasman Seas are important sources of moisture for rainfall across eastern Australia (*Stohl and James*, 2005; *Brown et al.*, 2009; *Gimeno et al.*, 2010). Prevailing easterlies transport this moisture onto the ESB, where orographic uplift promotes condensation and precipitation. The prevailing winds extend south during the summer months, as the sub-tropical ridge moves south, bringing rainfall to coastal tropical and sub-tropical areas. Enhanced onshore flow over the eastern coast maximises moisture availability and orographic rain (*Speer*, 2008; *Speer et al.*, 2009), and can often lead to heavy rain events (*Shepherd and Colquhoun*, 1985; *Hopkins and Holland*, 1997; *Speer and Leslie*, 2000). *Rakich et al.* (2008) developed the Gayndah-Deniliquin index (GDI), calculated as the difference in monthly-averaged sea level pressure between two surface stations (Figure 1), as a proxy for the strength of the zonal geostrophic wind flow across eastern Australia. The index was found to reach a maximum (i.e. strongest onshore flow) in March, and a minimum in September. While *Rakich et al.* (2008) found that the GDI has a strong relationship with summertime rainfall over eastern Australia, *Taschetto and England* (2009) showed that rainfall may also be influenced by trends at higher levels of the atmosphere, with ascending (descending) motion promoting (inhibiting) the convective formation of clouds.

Providing reliable climate projections across the ESB has been recognised as a difficult challenge (*Timbal*, 2010). This is because most current general circulation models have insufficient resolution to represent the complex topography of the region. This issue can be overcome, at least in part, by the application of statistical downscaling methods. Statistical downscaling involves developing quantitative relationships that link local variables (the 'predictands', e.g., precipitation) to synoptic scale forcing (the 'predictor') (*Wilby et al.*, 2004). The synoptic scale forcing of

a general circulation model can then be fed into this statistical model to estimate the local meteorological response, which is far less computationally expensive than dynamical downscaling (e.g., *Evans and McCabe*, 2013; *Mehrotra et al.*, 2014). This approach can be applied to predictions on a range of timescales (e.g., seasonal, inter-annual, decadal), but it is, of course, limited in future climate scenarios that differ significantly from the period used to determine the statistical relationships.

The central aim of this study is to build upon the work of *Rakich et al.* (2008) to develop a simple diagnostic (that we call the East Coast Flow Index, ECFI) that is able to best characterize the variability in summertime rainfall over the ESB. This is achieved by accounting for both the strength of the surface geostrophic flow along the eastern coastline, as well as the upper level circulation of the atmosphere. The ECFI is shown to have great potential as a predictor for statistically downscaling rainfall along the ESB as it is a physically-based index that is strongly correlated with rainfall, is capable of capturing multiyear variability, and is realistically represented by general circulation models.

The remainder of the paper is structured as follows: data and methods are discussed in Section 2, and the new index and the results are presented in Section 3. A follow-up discussion is presented in Section 4, commenting on new insights and perspectives brought by the index.

2 Data and Methods

For the purposes of this study the ESB is defined as the region between 25°–35°S and east of the Great Dividing Range (Figure 1). Rainfall observations are provided by the Australian Bureau of Meteorology Australian Water Availability Project (AWAP) rainfall dataset (*Jones et al.*, 2009). The AWAP rainfall dataset provides daily and monthly gridded rainfall fields extending back to 1900 on a 0.05° × 0.05° grid, and is highly regarded for studying rainfall trends and variability over eastern Australia (e.g., *Risbey et al.*, 2013; *King et al.*, 2013a,b). Daily and monthly fields

of mean sea level pressure (MSLP) and vertical motion (ω) from the NCEP/NCAR Reanalysis (*Kalnay et al.*, 1996)(hereafter NCEP) are used as a means of examining the mechanisms associated with the rainfall variability. Although there are some concerns with using NCEP data for investigating temporal trends (e.g., *Hines et al.*, 2000; *Sturaro*, 2003), the dataset has been deemed appropriate for use in a number of studies investigating atmospheric dynamics and Australian rainfall (e.g., *Hope et al.*, 2006; *Cai and Cowan*, 2008; *Taschetto and England*, 2009; *Verdon-Kidd and Kiem*, 2009; *Risbey et al.*, 2013). The advantage of NCEP data over other available reanalyses (e.g. ERA-Interim; *Dee et al.* 2011) is that it provides gridded data (2.5° × 2.5° resolution) from 1948 (instead of 1979) to present. Accordingly, this study examines observed summertime (1 December–28 February) rainfall from 1 December 1948.

In the first instance, AWAP and NCEP fields were used to examine composite atmospheric conditions associated with high and low summertime rainfall events over the ESB. The highest (lowest) 10% of region-averaged daily rainfall totals were used to define high (low) rainfall events, and the corresponding atmospheric composites were computed. These composites provided the basis for the derivation of the ECFI (Section 3.1). MSLP anomalies were calculated using the 1948–2012 base period. Once the ECFI was derived, zero-lag correlation coefficients were calculated between the index (calculated using NCEP data) and AWAP rainfall for daily, 7-day running average, monthly and seasonal fields. All time series in this study were linearly detrended prior to analysis to remove any relationship generated in the long-term trends. Throughout the study a significance level of 95% was used to decide if a relationship is significant.

Indices representing large-scale drivers of Australian precipitation were also used for comparison purposes. ENSO was represented by the Troup Southern Oscillation Index (SOI), which is the standardized anomaly of the MSLP difference between Tahiti and Darwin, multiplied by ten (*Troup*, 1965). SAM was represented by the station pressure index calculated by *Marshall* (2003), with monthly values available

from 1957 to present. As the IOD is most prominent in austral winter and spring (*Saji et al.*, 1999), its relationship to eastern Australian summertime rainfall was not investigated here. Each of the indices were correlated with rainfall as a means of comparison with the ECFI. The GDI is also examined using the official time series provided by the Australian Bureau of Meteorology. Throughout the study seasonal index values were taken as the average of monthly values.

In order to use the ECFI as a predictor for downscaling seasonal rainfall along the ESB, we must first build and validate the statistical model. Here we use a linear regression model in which observed rainfall is regressed against the reanalysis-derived ECFI at each AWAP grid point across the ESB. Validation of this statistical model was achieved through the use of split records: the period 1949-1980 is used for model calibration and the remaining period (1981-2012) for testing. This method is appropriate when long (>30-year) observation records are available (*Wilby et al.*, 2004). Following this initial testing the latter period of the NCEP/AWAP dataset (1981–2012) is used to calibrate the statistical model for application to the climate model.

As a means of investigating a potential application of the ECFI, the index was applied to climate model scenarios developed for the Australian region. This was achieved using a historical (1850–2005) and RCP8.5 future simulation (2006–2040) from the Australian Community Climate and Earth System Simulator 1.3 (ACCESS) coupled model submission to phase five of the Coupled Model Intercomparison Project (CMIP5; *Taylor et al.* 2012). A detailed description of this model and core CMIP5 simulations may be found in *Bi et al.* (2013) and *Dix et al.* (2013). We use the RCP8.5 experiment (Representative Concentration Pathway with high emissions for the 21st Century) as it is most representative of global CO_2 emissions from 2005 to present (*Peters et al.*, 2012). The Kolmogorov-Smirnov test was used to ascertain if the distributions of the ECFI (and its respective ω and pressure difference components) are realistically represented by the ACCESS model. Because the ECFI is a dynamical index and does not contain thermody-

namic quantities, it was not applied to the latter period of the RCP8.5 scenario as a means of reconstructing rainfall fields. This is because global temperatures at those times are expected to be several degrees warmer than current levels; due to the increased saturation vapour pressure and potential for higher moisture content under such conditions, thermodynamical factors would need to be considered when understanding the associated rainfall patterns and trends. Application of the ECFI to the ACCESS model data was by no means intended as an attempt to provide a robust evaluation of the model, or even as an assessment of modelled past and future rainfall variability. Rather, it was included to demonstrate a possible application of the index for more extensive future studies.

3 Results

3.1 The East Coast Flow Index

The composites of atmospheric conditions associated with ESB high and low daily summertime rainfall are shown in Figure 2. Surface winds can be inferred from the MSLP fields while vertical motion is represented by ω. For high rainfall events (Figures 2a and 2b), surface flow is directed onshore from the north-east. Negative (positive) MSLP anomalies along the eastern coastline near 20°S (40°S) suggests that the geostrophic flow, and hence onshore moisture advection from the Coral and Tasman Seas, is stronger than usual. The upper level disturbance is characterised by vertical ascent over the ESB (Figure 2a), providing an environment that would be conducive to the development of convection and clouds. Note that vertical cross-section of ω through the centre of the study domain (along 30°S) indicates that the vertical motion signal is strongest at around 500 hPa, 155°E. For low rainfall events (Figures 2c and 2d), the composite conditions are essentially the reverse of the high rainfall events: MSLP anomalies along the eastern coastline imply a weakened geostrophic flow and associated onshore moisture advection at the lower-levels of the

atmosphere, while there is large-scale upper-level descent. The maximum descent is located slightly higher and further offshore than the maximum ascent.

These high and low rainfall composites were used to define the *East Coast Flow Index* (ECFI), which is taken to be:

$$ECFI = \frac{(MSLP_{40°S,150°E} - MSLP_{20°S,150°E})}{\sigma(MSLP_{40°S,150°E} - MSLP_{20°S,150°E})} + \frac{-\omega_{500hPa,30°S,155°E}}{\sigma(\omega_{500hPa,30°S,155°E})} \quad (1)$$

The negative sign in front of the second term is used because negative values of ω infer ascent. As the two components of the ECFI are normalised the resulting index is unitless. Using this definition, the ECFI provides a measure of both the onshore flow (inferred from the MSLP gradient along the coastline) and vertical circulation (identified by ω). The position of the sampling points in equation 1 are guided by the meteorological conditions of Figure 2. Moreover, in the spirit of simplicity, latitudes and longitudes that are multiples of five are chosen. The longitude of 150°E is used for the MSLP gradient as it aligned with the study domain; the northern latitude point (20°S) coincides with the MSLP anomaly extrema while the southern point 40°S is located an an equal distance from the southern end of the study domain. The ω point is taken at 500 hPa, 30°S, 155°E to coincide with the locations identified in the composites with strong ω signals. The use of ω at 500 hPa provides a better account of ESB rainfall variability when compared to ω values taken at lower levels (see Appendix A). Importantly, the sampling points were deliberately positioned outside of the study domain to remove any local bias and to ensure that the resulting signal over the ESB is representative of the synoptic-scale flow. Experimentation found that these points provided the best correlation with ESB rainfall when compared against other grid-point combinations. Large, positive values of the ECFI infer strong onshore flow and vertical ascent over the ESB, while smaller/negative values represent weaker or reverse conditions that would result in an environment less favourable to rainfall.

3.2 Application of the ECFI to observational data

The ECFI is positively correlated with ESB summertime rainfall (>95% significance) for a range of different timescales (Figure 3). For daily values of the ECFI and rainfall, correlations are weak and of the order of 0.2–0.4 (Figure 3a). This is not a surprising finding as daily rainfall is a highly noisy signal and there are many days with zero rainfall. There is a marked increase in the correlation coefficients when the ECFI and rainfall are averaged over 7-day running periods (Figure 3b), with correlations reaching as high as 0.65 along the coast. The correlations are further strengthened when using monthly (Figure 3c) and seasonal (Figure 3d) fields. The location of the Great Dividing Range is particularly evident in the monthly and seasonal correlation fields; orographic enhancement of rainfall results in strong correlation values to the east of the Range, while there are weaker correlations in the lee (to the west) of the mountains. Hereafter the study will focus on the seasonal timescale.

The ECFI (equation 1) has two components - a measure of the surface pressure difference along the eastern coastline, and a measure of the upper-level vertical motion. Accordingly, these two components are separately related to eastern Australian rainfall variability (Figure 4). Correlations between seasonal values of the pressure difference (between 20°S and 40°S at 150°E) and rainfall results in strong correlations along the coastline (>0.6), particularly around the central latitudes of the ESB (Figure 4a). Correlations between the 500 hPa ω (at 30°S, 155°E) and rainfall clearly results in the highest correlations (>0.6) being achieved in the northern part of the ESB and further inland (Figure 4b). By combining these two components in the form of the ECFI, an overall better index of eastern Australian rainfall variability is achieved (Figure 3d). Therefore, when considering the ESB as an entity, rainfall variability is best explained by considering the synoptic flow in both the horizontal and vertical directions.

To compare the ECFI to other common indices, correlations between summer-

time rainfall and SOI (representing ENSO), SAM and the GDI are shown in Figure 5. Comparison of these maps with the ECFI equivalent (Figure 5d) highlights that the ECFI provides a better representation of ESB summertime rainfall variability. The GDI-rainfall correlations (Figure 5c) are weaker and less extensive than the equivalent correlations for both the ECFI (Figure 5d) and the pressure difference component of the ECFI (Figure 4a); this shows that the pressure sampling points of the ECFI (which are not constrained by surface station locations) better characterise the large scale zonal geostrophic wind anomalies over eastern Australia. While the ECFI has been designed for the summer period (December–February) it is still capable of performing well in the other seasons, especially spring (September–November)(Figure 6), maintaining markedly stronger correlations with ESB rainfall when compared to the SOI, SAM and GDI (see Appendix B for seasonal comparisons).

Although the ECFI provides stronger correlations with summertime rainfall across the ESB, it should be noted that it is not entirely independent of the two large-scale drivers - ENSO and SAM. For example, Table 1 shows that there are positive, statistically significant correlations between ECFI and each of SAM and SOI. A scatterplot of ECFI values plotted against their corresponding values of SOI and SAM (see Figure 7) reveals that larger (smaller) ECFI values generally occur when SAM and SOI are positive (negative). Accordingly, the ECFI is seen to combine the influence of these two large-scale drivers on rainfall, but with larger and more widespread significant correlations. The significant correlation between ECFI and the GDI (Table 1) is consistent with the fact that both indices provide a measure of the easterly geostrophic flow; however, the additional benefit of the ECFI to capture vertical motion over the ESB results in an overall improved index for characterizing rainfall variability (compare Figures 5c and 5d).

3.3 ECFI - a predictor for use in statistical downscaling

The results presented in Section 3.2 identify strong correlations between the large-scale flow (represented by the ECFI) and summertime rainfall along the ESB. That is, the ECFI provides a physical link between large-scale forcings and local precipitation responses. Accordingly, there is great potential for the ECFI to be incorporated into statistical downscaling models to provide local rainfall projections from the large-scale flow given by general circulation models. By way of testing this, the ability to reconstruct seasonal rainfall fields using the ECFI is first explored using observational data.

The downscaling model employed in this study involved fitting linear regressions between the ECFI and rainfall at each AWAP gridpoint along the ESB. These linear regressions were calculated using the AWAP rainfall and NCEP-derived ECFI values for the summer seasons of 1949–1980. For each of the remaining years of the observation record (1981–2012) the ECFI was applied to the downscaling model as a means of reconstructing the local rainfall fields. (Therefore the training/calibration period [1949–1980] is independent from the testing period [1981–2012]). The average of these reconstructed fields is shown in Figure 8a. The spatial patterns of the reconstructed rainfall closely resembles that of the AWAP observations for the same period (Figure 8b), with seasonal rainfall rates differing by less than 10% accross most of the ESB (Figure 8c). In particular, the reconstructed rainfall (Figure 8a) is able to reproduce much of the spatial variability in rainfall across the ESB, including the regions of local rainfall maxima near the coast. The temporal patterns of the observed and reconstructed rainfall fields along the ESB are shown in Figure 8d. While there are some differences between these time series it is clear that the ECFI is capable of representing interannual variations in rainfall.

The results of Figure 8 places confidence in the assumption that the relationship between the predictor and predictand remains valid for periods outside the calibration period. Moreover, it is important to note again that like other indices (ENSO,

SAM, GDI), the ECFI in a dynamical index only and does directly include thermodynamic quantities (e.g., temperature, water vapour). Nonetheless, in the above example the mean temperature between the training period and the reconstruction period is about 0.5°C, suggesting that the ECFI can be successfully applied, within reason, to future climate scenarios.

The reconstruction example demonstrates that there is scope for applying the ECFI to historical and future climate simulations of general circulation models as a means of developing possible higher resolution precipitation scenarios of the ESB, without the expense of dynamical downscaling. By way of example, the ECFI is applied to ACCESS model simulations. First and foremost, model-derived values of the ECFI (and its respective ω and pressure difference terms; see equation 1) are examined to ensure that they are adequately reproduced by the host model. Kolmogorov-Smirnov tests confirmed that there was no significant difference between the model- and NCEP-derived distributions; this result held true when considering both the model's historical and RCP8.5 simulation. Accordingly, we can be reasonably confident that the ACCESS model is able to represent the large-scale flow that is important for summertime rainfall variability.

Figure 9 shows the spatial correlations between the the ECFI and summertime rainfall for both the ACCESS historical and future simulations. Overall the model is successful in capturing the ECFI-rainfall relationship over eastern Australia. However, examination of the model's output rainfall field (Figure 10a) shows that the model does not have the spatial resolution to resolve the important influence of sub-grid topographic effects on ESB rainfall. By applying the model's ECFI values to the downscaling model previously described (as per Figure 8), except now using the 1981-2012 observations for the calibration period, a heterogeneous rainfall field is reconstructed (Figure 10b) that closely resembles the observed field (e.g., Figure 8b). These results identify a clear benefit in using the ECFI to downscale ESB rainfall from the model's large-scale flow.

The potential for the ECFI to be used for reconstructing possible climate sce-

narios is illustrated in Figure 10d. Here, ESB rainfall fields reconstructed for the period 2013–2040 are compared against those for 1981–2012. Both of these reconstructions use a statistical model calibrated from the 1981–2012 observations. (Note that here we limit the period to 2013–2040 because this restricts the mean temperature change to approximately 1°C). While this figure presents one possible climate scenario, it is included to show that the ECFI is capable of providing information on future projections at a spatial scale much finer that that of the global climate model (compare Figure 10c and 10d). Here the downscaled rainfall actually shows the largest increases in rainfall in regions where the raw climate model rainfall is shown to decrease. Indeed most of the (downscaled) rainfall increases coincide with regions of high climatological rainfall, consistent with the 'rich-get-richer' scenario. Finally, Figure 10e presents the time series of reconstructed ESB summer rainfall for the historical and future periods. The reconstructed rainfall patterns clearly display interannual and interdecadal variations that are not unlike that experienced in the AWAP observations.

4 Discussion and Conclusion

Many studies have examined Australian rainfall variability and its relationship to large-scale climate drivers and diagnostics. Although there are established relationships between these diagnostics and rainfall in the cooler seasons, the common indices used to represent those drivers poorly explain summertime rainfall variability in eastern Australia, especially along the coast (e.g., see *McBride and Nicholls*, 1983; *Risbey et al.*, 2009). Understanding rainfall along the eastern seaboard (ESB) is of particular importance, due to the large population and economic value of the region. It is also a region with strong topographic influence that cannot be well represented in current global climate models (*Timbal*, 2009).

This study builds upon the work of *Rakich et al.* (2008) to present a simple diagnostic that is able to best characterize summertime rainfall variability along

the ESB. With its derivation guided by composite synoptic conditions for high- and low-rainfall events, this simple yet effective East Coast Flow Index (ECFI) provides a measure of both the easterly geostrophic flow and vertical circulation over the ESB. The index infers easterly geostrophic flow from the meridional pressure gradient along the coastline, and vertical circulation from the upper-level ω field. High values of the index are achieved when there is strong onshore flow and vertical ascent over the ESB; this circulation would result in a moist environment that is favourable for the convective formation of clouds, and hence rainfall. In contrast, low values of the index represent conditions with reduced onshore flow and regional subsidence, which would inhibit convection and suppress precipitation. The index outperforms the common indices for drivers of rainfall variability, achieving statistically significant correlations with summertime rainfall across the ESB for a range of different timescales. While the ECFI has been designed for the summer period (December–February) it is shown to be capable of performing well in the other seasons, especially spring (September–November).

Although the ECFI provides stronger correlations with summer rainfall over the ESB when compared to large-scale climate drivers, it is not entirely independent of ENSO or SAM. Indeed, the ECFI combines the influence of these drivers, with higher (lower) values achieved when the SOI (representing ENSO) and the SAM are both positive (negative). This can be understood by relating the drivers to the large-scale dynamics that are characterised by the ECFI - that is, the onshore flow and vertical stability. It is well known that positive values of the SOI (La Niña periods) are associated with stronger trade winds and warmer SSTs to the north of Australia, providing an environment that favours vertical ascent and convective development; the reverse is generally true for negative values of the SOI (El Niño periods). Not surprisingly, La Niña (El Niño) periods are often associated with increased (decreased) rainfall over eastern Australia (*McBride and Nicholls*, 1983). During positive SAM events there is anomalous high pressure along the east coast at mid-latitudes (*Hendon et al.*, 2007), which would be expected to strengthen the

onshore winds further north. The findings of the current study are consistent with the work of *Rakich et al.* (2008), who found the northern pole of the GDI to be forced to a greater extent by ENSO, and the southern pole to be forced by the combined influence of ENSO and SAM. With all of this in mind, positive phases of both the SOI and SAM would be expected to result in enhanced onshore transport of moisture along the east coast, and an environment conducive to orographic uplift, condensation and precipitation. This would be consistent with a large ECFI value.

The results presented in this study demonstrate that the ECFI provides a physical link between large-scale forcings and local precipitation responses along the ESB. The study goes on to demonstrate that the ECFI has great potential for use in statistically downscaling the large scale-flow given by general circulation models to produce local rainfall projections. The ECFI is found to be adequately reproduced by the ACCESS climate model, which is a necessary precursor for the downscaling exercise (*Wilby et al.*, 2004). Validation of the statistical model by way of using split records demonstrated that the relationship between the predictor (ECFI) and predictand (precipitation) remained valid for periods outside the fitting period. The reconstructed rainfall fields from the ACCESS model closely resembled the observed rainfall fields for the period of overlap, and represented a marked improvement over the rainfall fields provided by the climate model. The reconstructed fields also display interannual and interdecadal variability, placing confidence in the use of the index for determining potential future climates. Moreover, the agreement between the distribution of the ECFI from a climate model and reanalyses data can be used to evaluate that model and, among other things, determine if that model should be used for (statistical or dynamical) downscaling of rainfall over the ESB.

Of course, as with other common indices, the ECFI is a purely dynamical index and does not contain thermodynamical quantities in its formulation. Accordingly, the ECFI may be limited for use in reconstructing rainfall for the latter periods of future climate simulations for which the global temperature is several degrees above present. In those scenarios, for example, the changes in precipitable water

could be large, which could affect the relationships between the ECFI and rainfall determined herein. Under such circumstances, thermodynamic quantities would need to be taken into consideration, which is beyond the scope of the current study. Nonetheless, as demonstrated here, the ECFI has significant potential for diagnosing and downscaling rainfall variability. Its application should be especially useful on timescales ranging from seasons through to a few decades, where changes in mean temperature differ by less than approximately 1°C from current climate. There is also scope to use the ECFI to better understand rainfall variations by isolating the effects of circulation changes on rainfall from those caused by changes in temperature and moisture.

This study has highlighted that the ECFI is a simple yet useful diagnostic. Given that the ESB is a region of social, economic and environmental significance there is an increasing need for the climate modelling community to provide future projections of rainfall on a spatial scale much finer than that provided by global or regional climate models. While it has long been a challenge to correctly simulate precipitation in climate models (*Dai*, 2006; *Stephens et al.*, 2010), this study has shown that the ECFI provides a credible means of inferring local ESB summer rainfall trends and variability from the large-scale flow. This statistical approach is complementary to dynamical downscaling approaches (e.g., *Evans and McCabe*, 2013; *Mehrotra et al.*, 2014). Application of the ECFI to the full suite of CMIP5 models is beyond the scope of this study and is an interesting topic for future research.

Acknowledgements

This work was funded by the Australian Research Council's Centre of Excellence for Climate System Science (CE110001028).

References

Ashok, K., Z. Guan, and T. Yamagata. 2003. Influence of the Indian Ocean Dipole on the Australian winter rainfall. *Geophysical Research Letters*, *30*, 1821. doi: 10.1029/2003GL017926.

Bi, D., et al. 2013. The ACCESS coupled model: Description, control climate and evaluation. *Australian Meteorological and Oceanographic Journal*, *63*, 41–64.

Brown, J. N., P. C. McIntosh, M. J. Pook, and J. S. Risbey. 2009. An investigation of the links between ENSO flavors and rainfall processes in southeastern Australia. *Monthly Weather Review*, *137*, 3786–3795. doi:10.1175/2009MWR3066.1.

Cai, W., and T. Cowan. 2008. Dynamics of late autumn rainfall reduction over southeastern Australia. *Geophysical Research Letters*, *35*, L09708. doi: 10.1029/2008GL033727.

Cai, W., T. Cowan, and A. Sullivan. 2009. Recent unprecedented skewness towards positive Indian Ocean Dipole occurrences and its impact on Australian rainfall. *Geophysical Research Letters*, *36*, L11705. doi:10.1029/2009GL037604.

Dai, A. 2006. Precipitation characteristics in eighteen coupled climate models. *Journal of Climate*, *19*, 4605–4630. doi:10.1175/JCLI3884.1.

Dee, D. P., et al. 2011. The ERA-Interim reanalysis: configuration and performance of the data assimilation system. *Quarterly Journal of the Royal Meteorological Society*, *137*, 553–597. doi:10.1002/qj.828.

Dix, M., et al. 2013. The ACCESS coupled model: documentation of core CMIP5 simulations and initial results. *Australian Meteorological and Oceanographic Journal*, *63*, 83–99.

Drosdowsky, W. 1993. An analysis of Australian seasonal rainfall anomalies: 1950–

1987. I: Spatial patterns. *International Journal of Climatology*, *13*, 1–30. doi: 10.1002/joc.3370130102.

Evans, J., and M. McCabe. 2013. Effect of model resolution on a regional climate model simulation over southeast Australia. *Climate Research*, *56*, 131–145. doi: 10.3354/cr01151.

Fenby, C., and J. Gergis. 2013. Rainfall variations in south-eastern Australia part 1: consolidating evidence from pre-instrumental documentary sources, 1788-1860. *International Journal of Climatology*, *33*. doi:10.1002/joc.3640.

Gallant, A. J. E., K. J. Hennessy, and J. S. Risbey. 2007. Trends in rainfall indices for six Australian regions: 1910-2005. *Australian Meteorological Magazine*, *56*, 223–239.

Gergis, J., and L. Ashcroft. 2013. Rainfall variations in south-eastern Australia part 2: a comparison of documentary, early instrumental and palaeoclimate records, 1788-2008. *International Journal of Climatology*, *33*. doi:10.1002/joc.3639.

Gimeno, L., A. Drumond, R. Nieto, R. M. Trigo, and A. Stohl. 2010. On the origin of continental precipitation. *Geophysical Research Letters*, *37*, L13804. doi: 10.1029/2010GL043712.

Hendon, H. H., D. W. J. Thompson, and M. C. Wheeler. 2007. Australian rainfall and surface temperature variations associated with the Southern Hemisphere Annular Mode. *Journal of Climate*, *20*, 2452–2467. doi:10.1175/JCLI4134.1.

Hines, K. M., D. H. Bromwich, and G. J. Marshall. 2000. Artificial surface pressure trends in the NCEP-NCAR Reanalysis over the Southern Ocean and Antarctica. *Journal of Climate*, *13*, 3940–3952.

Hope, P. K., W. Drosdowsky, and N. Nicholls. 2006. Shifts in the synoptic systems influencing southwest Western Australia. *Climate Dynamics*, *26*, 751–764. doi: 10.1007/s00382-006-0115-y.

Hopkins, L. C., and G. J. Holland. 1997. Australian heavy-rain days and associated east coast cyclones: 1958-92. *Journal of Climate*, *10*, 621–635.

Jones, D., W. Wang, and R. Fawcett. 2009. High-quality spatial climate data-sets for Australia. *Australian Meteorological and Oceanographic Journal*, *58*, 233–248.

Kalnay, E., et al. 1996. The NCEP/NCAR 40-Year Reanalysis Project. *Bulletin of the American Meteorological Society*, *77*, 437–471.

King, A. D., L. V. Alexander, and M. G. Donat. 2013a. Asymmetry in the response of Eastern Australia extreme rainfall to low-frequency Pacific variability. *Geophysical Research Letters*, *40*, 2271–2277. doi:10.1002/grl.50427.

King, A. D., L. V. Alexander, and M. G. Donat. 2013b. The efficacy of using gridded data to examine extreme rainfall characteristics: a case study for Australia. *International Journal of Climatology*, *33*, 2376–2387. doi:10.1002/joc.3588.

Marshall, G. 2003. Trends in the Southern Annular Mode from observations and reanalyses. *Journal of Climate*, *16*, 4134–4143.

McBride, J. L., and N. Nicholls. 1983. Seasonal relationships between Australian rainfall and the Southern Oscillation. *Monthly Weather Review*, *111*, 1998–2004.

Mehrotra, R., J. P. Evans, A. Sharma, and B. Sivakumar. 2014. Evaluation of downscaled daily rainfall hindcasts over Sydney, Australia using statistical and dynamical downscaling approaches. *Hydrology Research*, *45*, 226–249. doi: 10.2166/nh.2013.094.

Meneghini, B., I. Simmonds, and I. N. Smith. 2007. Association between Australian rainfall and the Southern Annular Mode. *International Journal of Climatology*, *27*, 109–121. doi:10.1002/joc.1370.

Nicholls, N. 2010. Local and remote causes of the southern Australian autumn-winter rainfall decline, 1958-2007. *Climate Dynamics*, *34*, 835–845. doi:10.1007/s00382-009-0527-6.

Nicholls, N., B. Lavery, C. Frederiksen, W. Drosdowsky, and S. Torok. 1996. Recent apparent changes in relationships between the El Niño-Southern Oscillation and Australian rainfall and temperature. *Geophysical Research Letters*, *23*, 3357–3360. doi:10.1029/96GL03166.

Nicholls, N., W. Drosdowsky, and B. Lavery. 1997. Australian rainfall variability and change. *Weather*, *52*, 66–72. doi:10.1002/j.1477-8696.1997.tb06274.x.

Pepler, A., A. Coutts-Smith, and B. Timbal. 2014. The role of East Coast Lows on rainfall patterns and inter-annual variability across the East Coast of Australia. *International Journal of Climatology*, *34*, 1011–1021. doi:10.1002/joc.3741.

Peters, G. P., R. M. Andrew, T. Boden, J. G. Canadell, P. Ciais, C. L. Quéré, G. Marland, M. R. Raupach, and C. Wilson. 2012. The challenge to keep global warming below 2^{o}C. *Nature Climate Change*, *3*, 4–6. doi:10.1038/nclimate1783.

Rakich, C. S., N. J. Holbrook, and B. Timbal. 2008. A pressure gradient metric capturing planetary-scale influences on eastern Australian rainfall. *Geophysical Research Letters*, *35*, L08713. doi:10.1029/2007GL032970.

Risbey, J. S., M. J. Pook, P. C. McIntosh, M. C. Wheeler, and H. H. Hendon. 2009. On the remote drivers of rainfall variability in Australia. *Monthly Weather Review*, *137*, 3233–3253. doi:10.1175/2009MWR2861.1.

Risbey, J. S., P. C. McIntosh, and M. J. Pook. 2013. Synoptic components of rainfall variability and trends in southeast Australia. *International Journal of Climatology*, *33*, 2459–2472. doi:10.1002/joc.3597.

Saji, N. H., B. N. Goswami, P. N. Vinayachandran, and T. Yamagata. 1999. A dipole mode in the tropical Indian Ocean. *Nature*, *401*, 360–363. doi:10.1038/43854.

Shepherd, D. J., and J. R. Colquhoun. 1985. Meteorological aspects of an extraordinary flash flood event near Dapto, New South Wales. *Australian Meteorological Magazine*, *33*, 87–102.

Speer, M., L. Leslie, and A. Fierro. 2009. Australian east coast rainfall decline related to large scale climate drivers. *Climate Dynamics*, *36*, 1419–1429. doi: 10.1007/s00382-009-0726-1.

Speer, M. S. 2008. On the late twentieth century decrease in Australian east coast rainfall extremes. *Atmospheric Science Letters*, *9*, 160–170. doi:10.1002/asl.191.

Speer, M. S., and L. M. Leslie. 2000. A comparison of five flood rain events over the New South Wales north coast and a case study. *International Journal of Climatology*, *20*, 543–563.

Stephens, G. L., T. L'Ecuyer, R. Forbes, A. Gettlemen, J.-C. Golaz, A. Bodas-Salcedo, K. Suzuki, P. Gabriel, and J. Haynes. 2010. Dreary state of precipitation in global models. *Journal of Geophysical Research: Atmospheres*, *115*, D24211. doi:10.1029/2010JD014532.

Stohl, A., and P. James. 2005. A Lagrangian analysis of the atmospheric branch of the global water cycle. Part II: Moisture transports between Earth's ocean basins and river catchments. *Journal of Hydrometeorology*, *6*, 961–984. doi: 10.1175/JHM470.1.

Sturaro, G. 2003. A closer look at the climatological discontinuities present in the NCEP/NCAR reanalysis temperature due to the introduction of satellite data. *Climate Dynamics*, *21*, 309–316. doi:10.1007/s00382-003-0334-4.

Taschetto, A. S., and M. H. England. 2009. An analysis of late twentieth century trends in Australian rainfall. *International Journal of Climatology*, *29*, 791–807. doi:10.1002/joc.1736.

Taylor, K. E., R. J. Stouffer, and G. A. Meehl. 2012. An Overview of CMIP5 and the Experiment Design. *Bulletin of the American Meteorological Society*, *93*, 485–498. doi:10.1175/BAMS-D-11-00094.1.

Timbal, B. 2009. The continuing decline in southeast Australian rainfall: update to May 2009. *CAWCR Research Letters*, *5*, 1–8.

Timbal, B. 2010. The climate of the Eastern Seaboard of Australia: A challenging entity now and for future projections. *IOP Conference Series: Earth and Environmental Science*, *11*, 12013. doi:10.1088/1755-1315/11/1/012013.

Troup, A. J. 1965. The southern oscillation. *Quarterly Journal of the Royal Meteorological Society*, *91*, 490–506. doi:10.1002/qj.49709139009.

Ummenhofer, C. C., M. H. England, P. C. McIntosh, G. A. Meyers, M. J. Pook, J. S. Risbey, A. S. Gupta, and A. S. Taschetto. 2009. What causes southeast Australia's worst droughts? *Geophysical Research Letters*, *36*, L04706. doi:10.1029/2008GL036801.

Verdon-Kidd, D. C., and A. S. Kiem. 2009. On the relationship between large-scale climate modes and regional synoptic patterns that drive Victorian rainfall. *Hydrology and Earth System Sciences*, *13*, 467–479. doi:10.5194/hess-13-467-2009.

Wang, G., and H. H. Hendon. 2007. Sensitivity of Australian rainfall to inter-El Niño variations. *Journal of Climate*, *20*, 4211–4226. doi:10.1175/JCLI4228.1.

Wilby, R. L., S. P. Charles, E. Zorita, B. Timbal, P. Whetton, and L. O. Mearns, Guidelines for Use of Climate Scenarios Developed from Statistical Downscaling Methods, *Tech. Rep. August*, 2004.

Tables

Table 1: Correlations between detrended summertime time series of the ECFI and each of SAM, SOI and GDI. All correclations are significant (at the 95% level). Correlations are computed using seasonal values starting in 1957, when the SAM index becomes available.

	SAM	SOI	GDI
ECFI	0.58	0.53	0.57

Figure Captions

Figure 1. Average summer rainfall rates (1949–2012) from the Australian Bureau of Meteorology Australian Water Availability Project rainfall dataset (*Jones et al.*, 2009). The 'eastern seaboard' region is outlined in red. The Great Dividing Range escarpment is represented by thick hatchings, while the locations of Gayndah and Deniliquin are identified by the letters G and D, respectively.

Figure 2. Composite atmospheric conditions for Australian eastern seaboard high rainfall events (a and b) and low rainfall events (c and d). Maps of Mean Sea Level Pressure (hPa; contours), MSLP anomalies (hPa; shaded) and 500 hPa ω (Pa/s; stippling identifies region of vetical ascent) are shown in (a) and (c). The thick dashed lines in (a) and (c) identify the locations of the vertical cross-sections of ω (Pa/s; negative values infer ascent), which are shown in (b) and (d) respectively.

Figure 3. Maps of correlation coefficients between the ECFI and observed summertime rainfall. Correlations are computed using (a) daily, (b) 7-day running average, (c) monthly and (d) seasonal fields, over the period 1 December 1948 – 28 February 2012. Only correlations significant at the 95% confidence level and above are shown. H identifies the strongest positive point correlation value within the eastern seaboard region.

Figure 4. Maps of correlation coefficients between observed summertime rainfall and (a) the surface pressure difference between 20°S and 40°S at 150°E, and (b) the 500 hPa ω ($\times$ -1) at 30°S, 155°E. Correlations are computed using seasonal values over the period 1 December 1948 – 28 February 2012. Only correlations significant at the 95% confidence level and above are shown. H identifies the strongest positive point correlation value within the eastern seaboard region.

Figure 5. As per Figure 4, but for correlation between observed summertime rainfall and (a) SOI (representing ENSO), (b) SAM, (c) GDI and (d) ECFI. Correlations with SAM commence in December 1957, when the index first becomes available.

Figure 6. As per Figure 3d, but for correlations between the ECFI and observed seasonal rainfall in (a) MAM, (b) JJA and (c) SON.

Figure 7. Scatterplot of seasonal ECFI values (DJF, 1958–2012) in terms of the SAM and SOI index. Marker size is indicative of the magnitude of the ECFI; positive (negative) ECFI values are shown in red (blue).

Figure 8. (a) Average summer rainfall reconstructed for the period 1981-2012 using the ECFI from the NCEP renalysis. (b) Observed summer rainfall for the same period. (c) The difference between the reconstructed and observed fields, expressed as a percentage of the observed field. (d) Time series of eastern seaboard area-average DJF rainfall for the observed and reconstructed fields.

Figure 9. Spatial correlations between the ECFI and summertime rainfall as represented by the ACCESS model for the (a) DJF 1981–2012 and (b) DJF 2013–2040. Only correlations significant at the 95% confidence level and above are shown.

Figure 10. (a) Average summer rainfall (1981–2012) from the ACCESS model. (b) Rainfall for the same period reconstructed using the ECFI from the ACCESS model. (c) Projected change in rainfall for 2013–2040 relative to 1981–2012, as identified by the ACCESS model. (d) As per (c), but reconstructed from the ACCESS model using the ECFI. (e) Time series of eastern seaboard area-average DJF rainfall reconstructed from the ACCESS simulations. Observed (AWAP) DJF rainfall is also shown. Thinner lines indicate seasonal values while thicker lines represent 10-year centred moving averages.

Figures

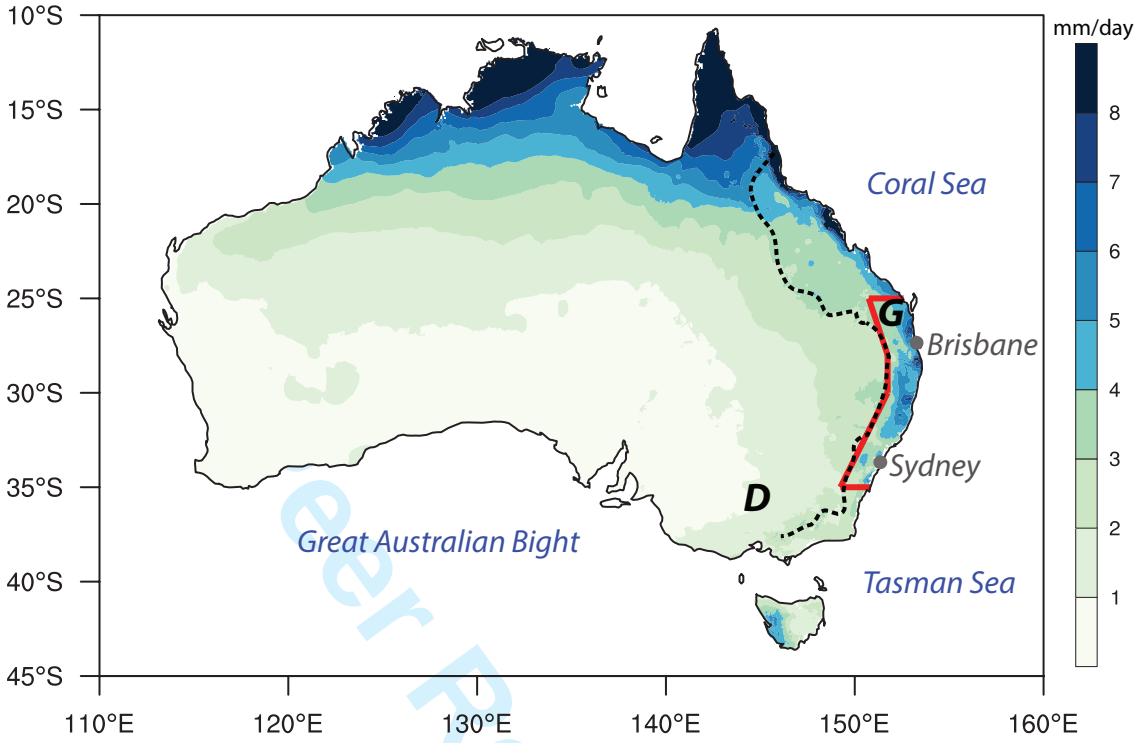

Figure 1: Average summer rainfall rates (1949–2012) from the Australian Bureau of Meteorology Australian Water Availability Project rainfall dataset (*Jones et al.*, 2009). The 'eastern seaboard' region is outlined in red. The Great Dividing Range escarpment is represented by thick hatchings, while the locations of Gayndah and Deniliquin are identified by the letters G and D, respectively.

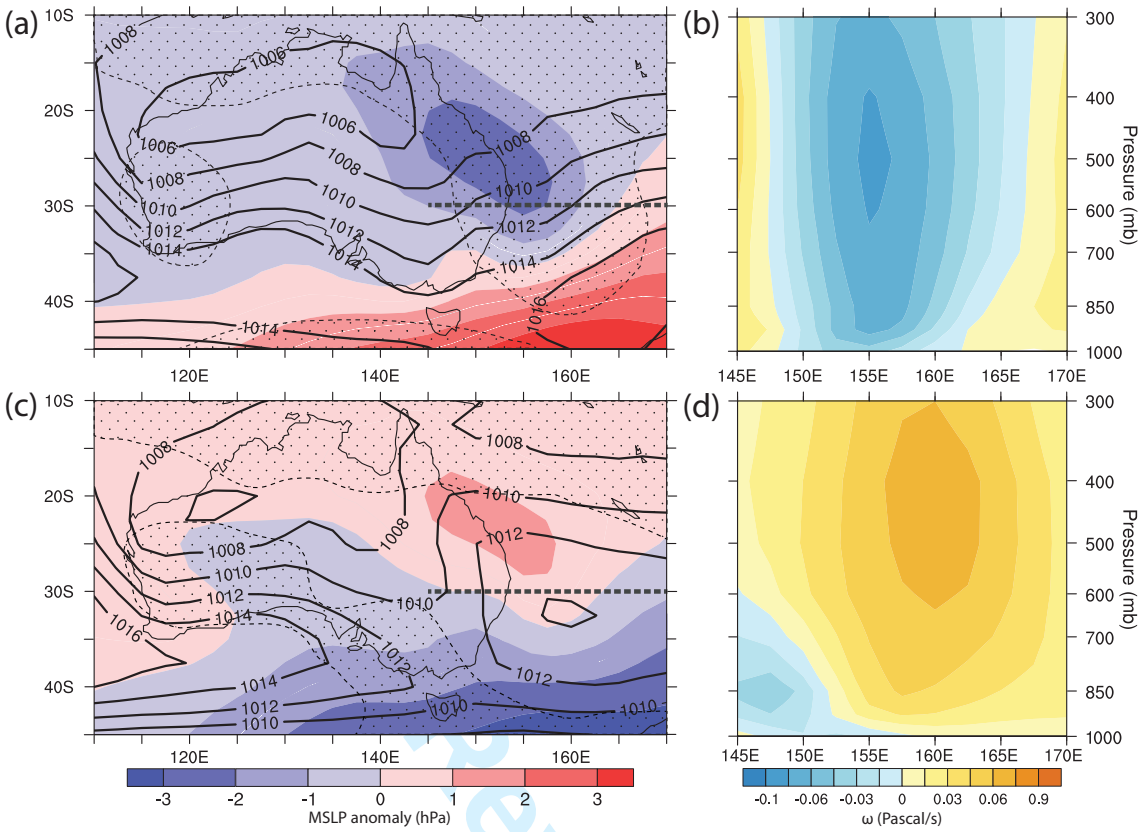

Figure 2: Composite atmospheric conditions for Australian eastern seaboard high rainfall events (a and b) and low rainfall events (c and d). Maps of Mean Sea Level Pressure (hPa; contours), MSLP anomalies (hPa; shaded) and 500 hPa ω (Pa/s; stippling identifies region of vetical ascent) are shown in (a) and (c). The thick dashed lines in (a) and (c) identify the locations of the vertical cross-sections of ω (Pa/s; negative values infer ascent), which are shown in (b) and (d) respectively.

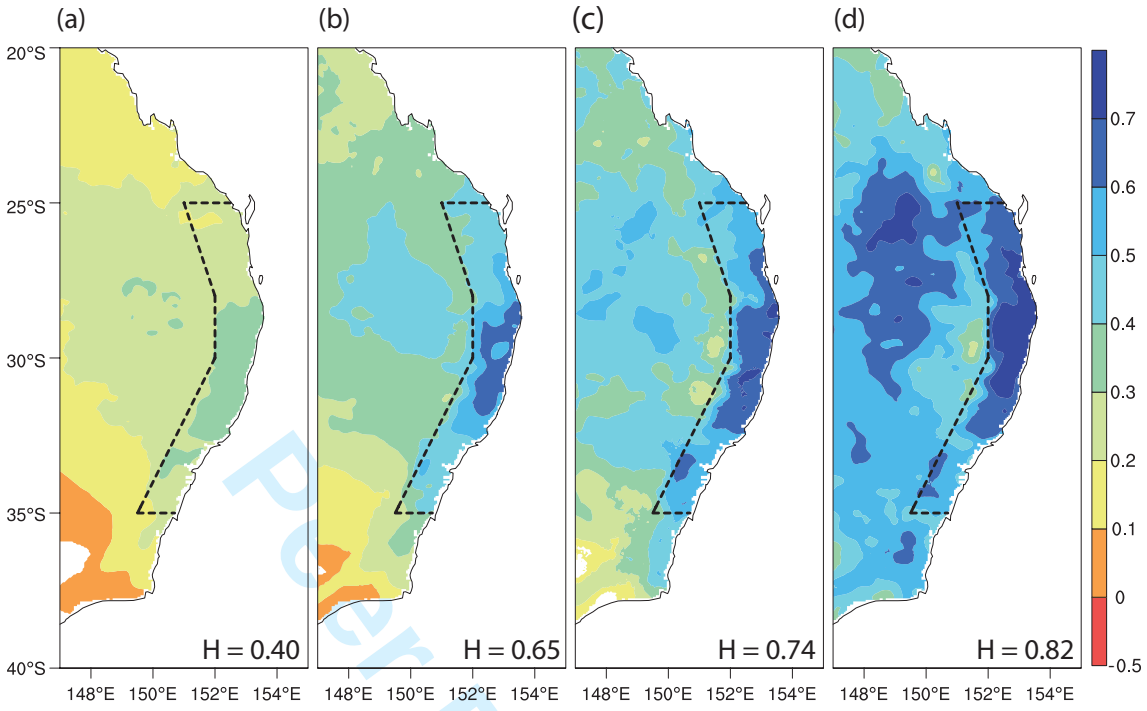

Figure 3: Maps of correlation coefficients between the ECFI and observed summertime rainfall. Correlations are computed using (a) daily, (b) 7-day running average, (c) monthly and (d) seasonal fields, over the period 1 December 1948 – 28 February 2012. Only correlations significant at the 95% confidence level and above are shown. H identifies the strongest positive point correlation value within the eastern seaboard region.

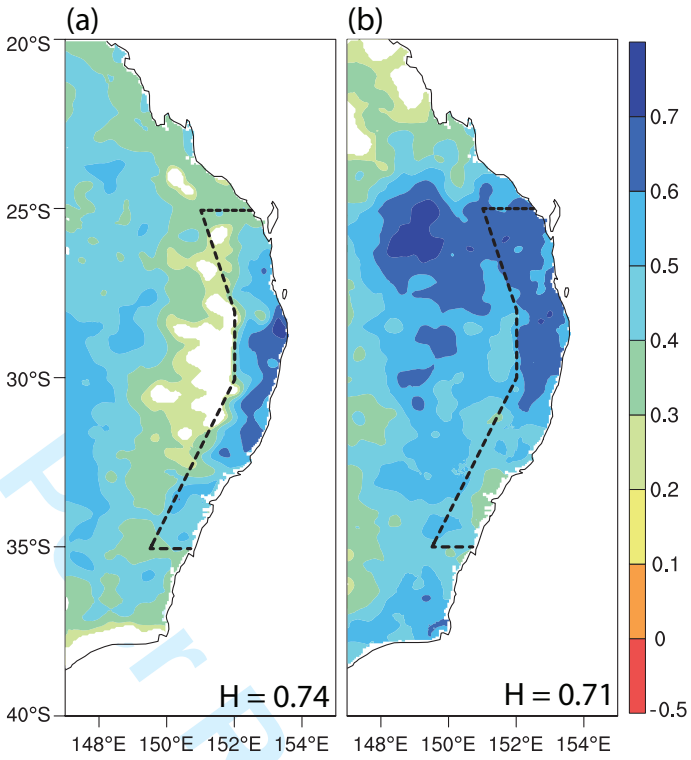

Figure 4: Maps of correlation coefficients between observed summertime rainfall and (a) the surface pressure difference between 20°S and 40°S at 150°E, and (b) the 500 hPa ω ($\times$ -1) at 30°S, 155°E. Correlations are computed using seasonal values over the period 1 December 1948 – 28 February 2012. Only correlations significant at the 95% confidence level and above are shown. H identifies the strongest positive point correlation value within the eastern seaboard region.

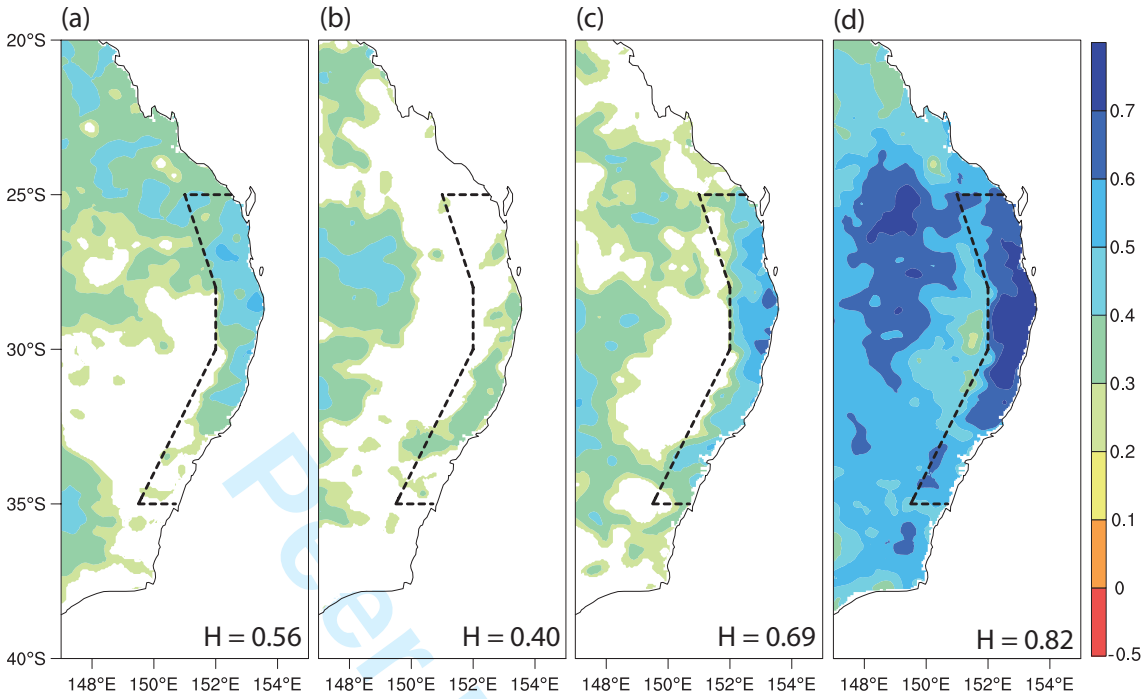

Figure 5: As per Figure 4, but for correlation between observed summertime rainfall and (a) SOI (representing ENSO), (b) SAM, (c) GDI and (d) ECFI. Correlations with SAM commence in December 1957, when the index first becomes available.

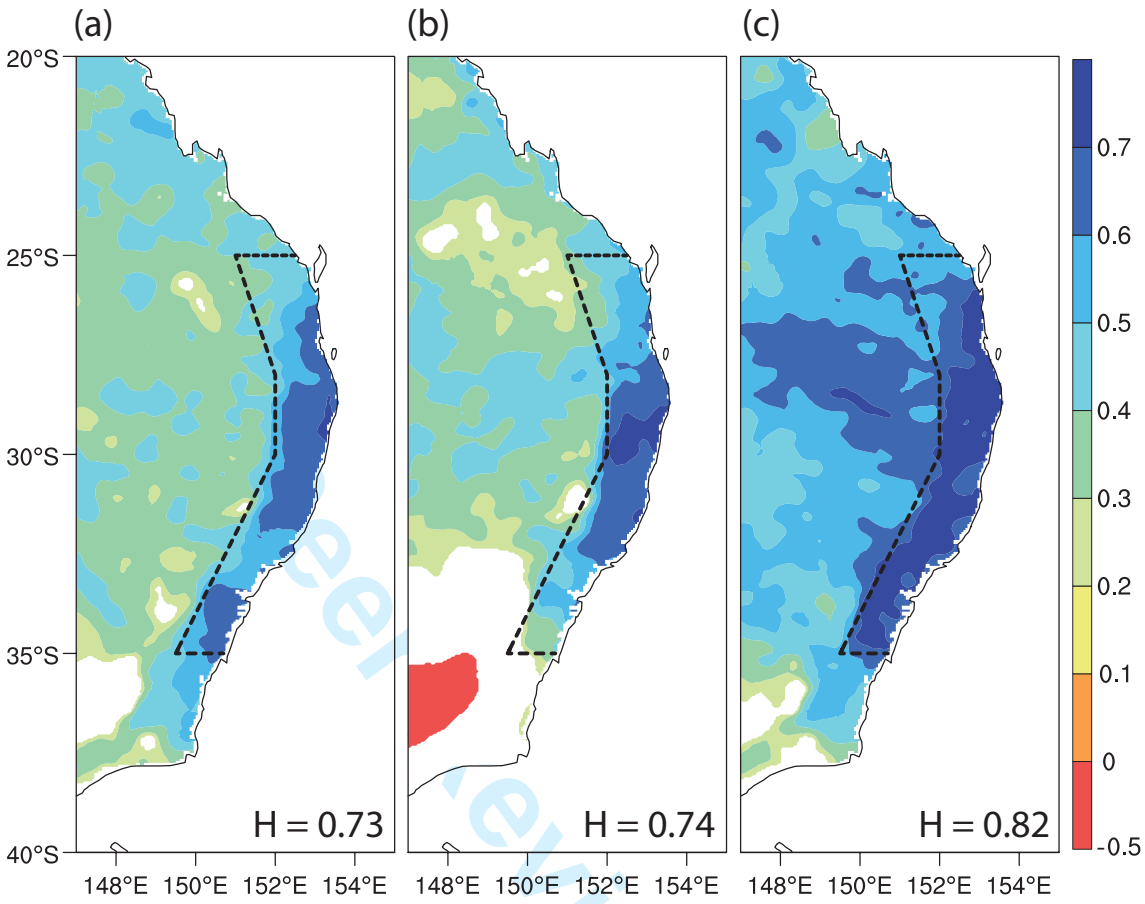

Figure 6: As per Figure 3d, but for correlations between the ECFI and observed seasonal rainfall in (a) MAM, (b) JJA and (c) SON.

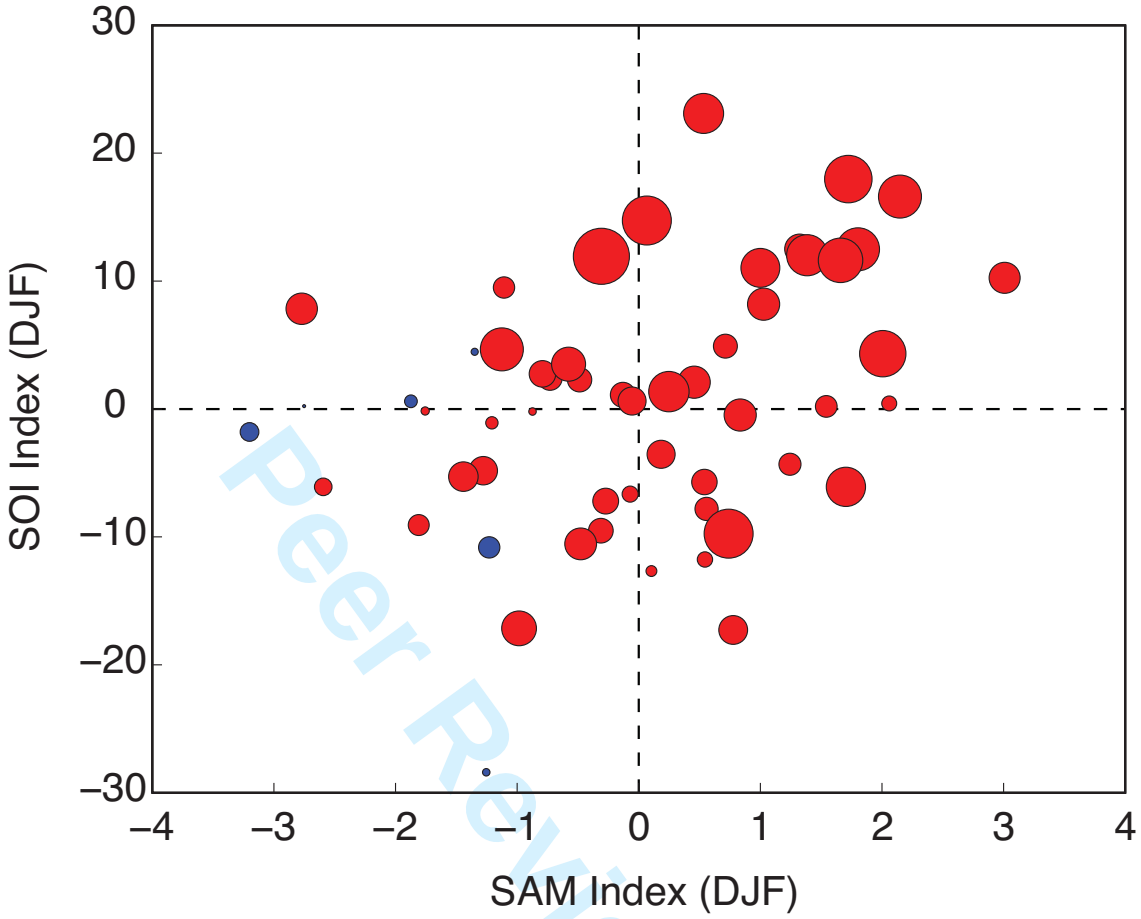

Figure 7: Scatterplot of seasonal ECFI values (DJF, 1958–2012) in terms of the SAM and SOI index. Marker size is indicative of the magnitude of the ECFI; positive (negative) ECFI values are shown in red (blue).

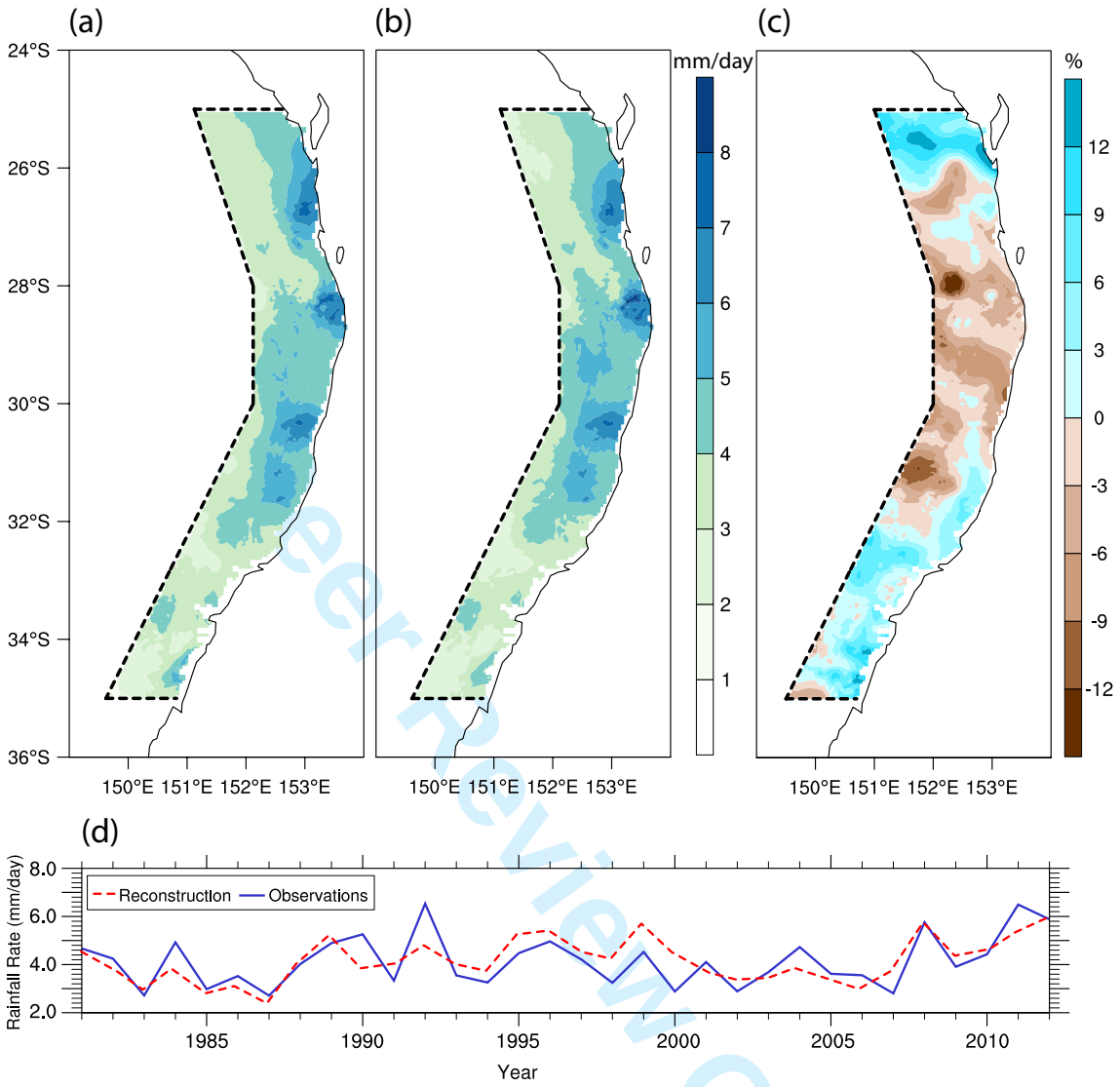

Figure 8: (a) Average summer rainfall reconstructed for the period 1981-2012 using the ECFI from the NCEP renalysis. (b) Observed summer rainfall for the same period. (c) The difference between the reconstructed and observed fields, expressed as a percentage of the observed field. (d) Time series of eastern seaboard area-average DJF rainfall for the observed and reconstructed fields.

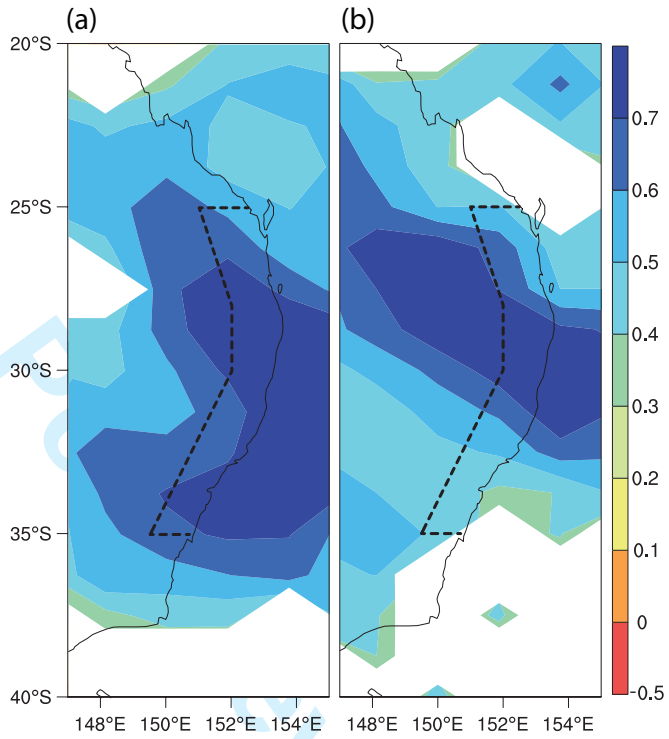

Figure 9: Spatial correlations between the ECFI and summertime rainfall as represented by the ACCESS model for the (a) DJF 1981–2012 and (b) DJF 2013–2040. Only correlations significant at the 95% confidence level and above are shown.

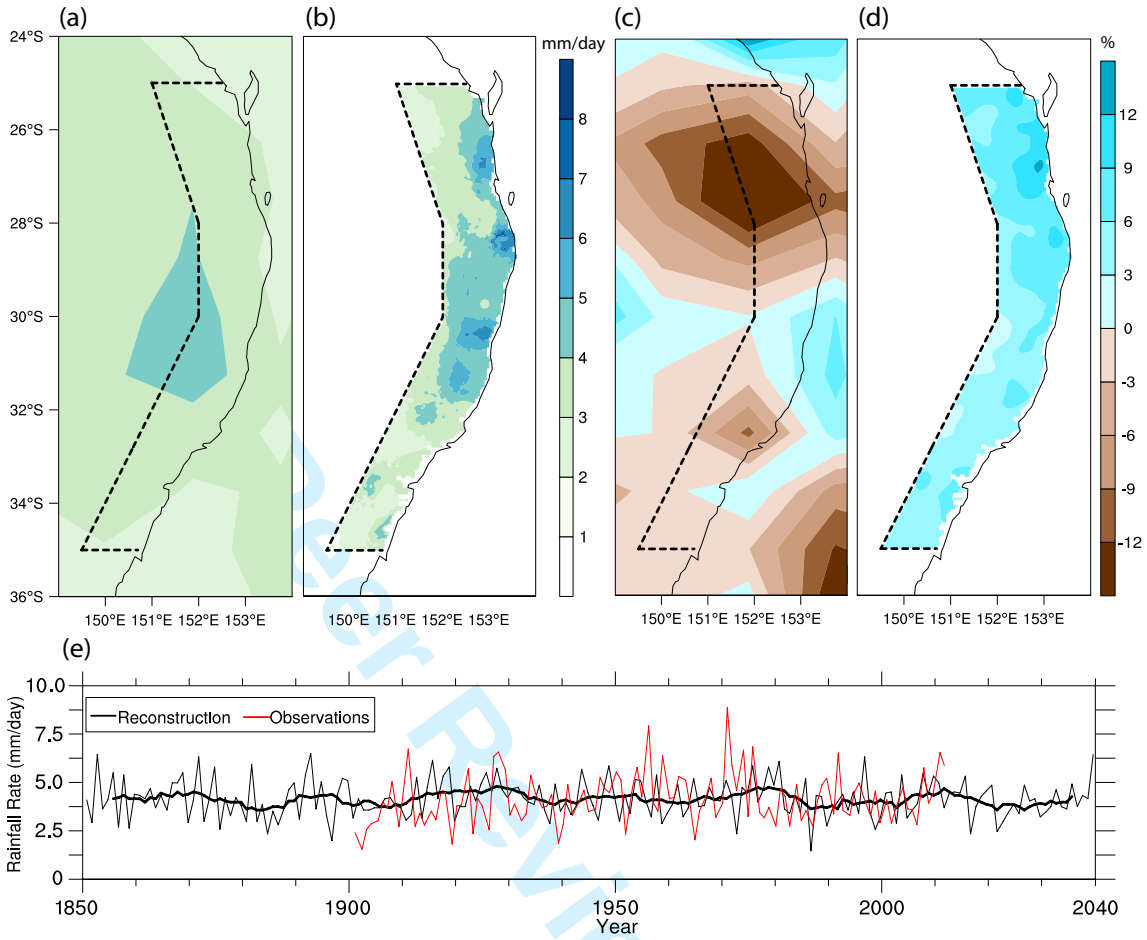

Figure 10: (a) Average summer rainfall (1981–2012) from the ACCESS model. (b) Rainfall for the same period reconstructed using the ECFI from the ACCESS model. (c) Projected change in rainfall for 2013–2040 relative to 1981–2012, as identified by the ACCESS model. (d) As per (c), but reconstructed from the ACCESS model using the ECFI. (e) Time series of eastern seaboard area-average DJF rainfall reconstructed from the ACCESS simulations. Observed (AWAP) DJF rainfall is also shown. Thinner lines indicate seasonal values while thicker lines represent 10-year centred moving averages.